



Contents lists available at ScienceDirect

## Corrosion Science

journal homepage: [www.elsevier.com/locate/corsci](http://www.elsevier.com/locate/corsci)

# Corrosion of copper and steel alloys in a simulated underground storage-tank sump environment containing acid-producing bacteria <sup>☆</sup>

Jeffrey W. Sowards <sup>\*</sup>, Elisabeth Mansfield

Applied Chemicals and Materials Division, National Institute of Standards and Technology, 325 Broadway, Boulder, CO 80305, USA

## ARTICLE INFO

## Article history:

Received 7 January 2014

Accepted 7 July 2014

Available online xxxx

## Keywords:

C. Atmospheric corrosion

A. Carbon steel

A. Copper

C. Microbiological corrosion

B. Weight loss

## ABSTRACT

We simulate corrosion observed in underground fuel storage tank systems by headspace and aqueous exposure to biotic organic acid. Carbon steel and copper were exposed to *Acetobacter* sp. inoculated into aqueous-ethanol solutions over a period of approximately 30 days. The steel alloy exhibited pitting corrosion and the copper alloy exhibited pitting and intergranular corrosion due to acetic acid produced by the microbes. Corrosion rates were dependent on formation of corrosion products and are ranked as follows in order of increasing magnitude: Copper-aqueous < Steel-aqueous < Copper-headspace < Steel-headspace. The laboratory test method developed here reproduces corrosion observed in practice.

Published by Elsevier Ltd.

## 1. Introduction

Production and consumption rates of ethanol, biodiesel fuel, and other alternative fuels are projected to increase significantly in the U.S. in the coming years [1]. Usage of ethanol as an additive to gasoline is already quite high. In as recently as 2010, over 90% of the gasoline sold in the U.S. was reportedly blended with ethanol [2]. However, much of the current fuel infrastructure was designed for unblended gasoline, and there is growing concern that some of the materials used in the past may not be compatible with the emerging blended fuels [3,4]. One of the main concerns regarding material incompatibility is the potential for corrosion of fuel storage and dispensing infrastructure, which may result in leakage of fuels and subsequent pollution of the ground water supply requiring expensive clean-up and mitigation.

Since as early as 2008, inspectors in nine different U.S. states have reported an increasing number of incidents where underground storage tank (UST) components exhibited sudden and rapid corrosion [5]. The UST components that exhibited unexpected corrosion included sump pumps, submersible turbine pumps, risers, and ventilation pipes. Measurements of headspace chemistry revealed that high ethanol-vapor concentrations were associated with the corrosion, although the occurrence of corrosion was not exclusive to storage scenarios involving ethanol-blended gasoline

fuels. The presence of acetic acid (measured in the form of acetate) and microbiological activity in the sump-pump environments was noted where corrosion occurred. Rapid corrosion of UST components associated with handling and dispensing of ultra-low-sulfur diesel (ULSD) fuels has also occurred [6]. In fuel storage scenarios involving ULSD, ethanol contamination was observed at many of the UST test sites [6]. The U.S. Environmental Protection Agency analyzed UST sump waters and vapors from many locations across the U.S., finding that high acetate concentrations ( $>1000 \text{ mg L}^{-1}$ ) were associated with the presence of ethanol in a variety of ethanol-blended gasoline and other fuels [7]. The levels of acetate were correlated to rust tubercles on steel and blue corrosion product on copper [7]. Analysis of all the UST components revealed the presence of acetic acid-producing bacteria (e.g., *Acetobacter* sp.) [5–7], a class of common microorganism that converts ethanol to acetic acid. These microorganisms likely caused or contributed to the accelerated corrosion [5–7] and were even identified as the predominant microbes found in the ULSD fuel systems [6].

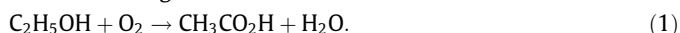
Microbiologically-influenced corrosion (MIC) and microbial contamination have been associated with the usage and distribution of various liquid fuels for many years [8,9] and thus are not new problems in fuel-handling and dispensing scenarios. With respect to ethanol fuel in particular, industrial storage tanks have reportedly sustained microbial life including acid-producing bacteria (APB) and sulfate-reducing bacteria (SRB) [10]. APB, including *Acetobacter* sp., secrete organic acids during the fermentation of organic compounds, and are known to influence corrosion of metals [11]. *Acetobacter* sp. in particular, oxidize ethanol during the

<sup>☆</sup> Contribution of NIST, an agency of the U.S. government. Not subject to copyright.

<sup>\*</sup> Corresponding author. Tel.: +1 303 497 7960.

E-mail address: [jeffrey.sowards@nist.gov](mailto:jeffrey.sowards@nist.gov) (J.W. Sowards).

fermentation process, resulting in acetic-acid production according to the following reaction:



APB have been shown to promote localized corrosion of steels at inclusion sites where the observed corrosion damage exhibits a distinct appearance from corrosion produced by a protic acid of the same pH [12]. Acetic acid is known to corrode metals while in its vapor form and when dissolved in an aqueous solution. Biotic acetic acid vapor that emanated from wood samples was shown to influence corrosion of copper, lead, and brass coupons [13]; however, most corrosion experiments to-date have considered acetic acid from abiotic sources. Abiotic acetic acid vapor has been shown to promote the corrosion of copper [14] and mild steel [15,16], which are two metallic materials used in mechanical components exposed to fuel vapors and aqueous phases contained in UST sump systems. The corrosion rate of mild steel exposed to aqueous mixtures of acetic acid was found to be quite high, and exhibited dependence on acid concentration, temperature, and the period of exposure [17]. The rate of copper corrosion exposed to aqueous acetic acid solutions was shown to be dependent on acid concentration [18], and was strongly influenced by relative humidity when exposed to acetic acid vapor [19].

This work reports on a corrosion evaluation study performed with a new testing methodology developed to simulate the MIC observed in UST systems. A headspace testing chamber was designed so that corrosion of sump-pump component alloys could be evaluated during exposure to ethanol and acetic-acid vapor components. *Acetobacter aceti* were used here to generate acetic acid in a simulated ethanol fuel environment to confirm that MIC is a plausible mechanism for the corrosion seen on UST sump-pump components. The biotic source of acetic acid is critical since abiotic substitutes might not replicate corrosion induced by microbes [12]. The use of *A. aceti* also provides information on biological properties (e.g., bacterial attachment) that would not be achieved with the addition of acetic acid solution alone. This test, while it did not incorporate blended fuels (e.g., E15, E85), could prove useful in evaluating MIC in fuel samples collected from field studies, including non-ethanol blended fuels. Furthermore, the test method could prove useful in investigating the growing number of microbes in fuels and crude oils that may be contributing to biodegradation of fuels and fuel infrastructure [20,21].

## 2. Materials and methods

### 2.1. Materials

Two rod alloys (19.05 mm diameter) were obtained for this study from a commercial vendor, including a Type 1018 cold-drawn steel rod conforming to ASTM A108 specifications [22] and an Alloy 110 (H04 hard temper) copper rod conforming to ASTM B187 specifications [23]. Chemical compositions of both materials are reported in Table 1. Metal rods were saw-cut into disk-shaped coupons with a thickness of approximately 2.8 mm for corrosion tests.

### 2.2. Bacterial growth

Environmental isolates of *A. aceti* were cultivated from a fueling terminal tank [24]; samples were identified by 16S rRNA gene

sequencing. *A. aceti* were maintained in a medium containing yeast extract (0.5 g L<sup>-1</sup>), peptone (0.3 g L<sup>-1</sup>), and sodium chloride (1 g L<sup>-1</sup>) in distilled water [25] at pH 6. Ethanol (5% by volume) was added as a carbon source. A concentrated *Acetobacter* culture was established by growing the bacteria in 100 mL of culture media for 1 week. This established culture, which is in a stationary phase, was diluted for headspace experiments.

### 2.3. Preparation of headspace chambers

Saw-cut coupons were prepared according to ASTM G-1 Standard Practice for Preparing, Cleaning, and Evaluating Corrosion Test Specimens [26]. Coupons were progressively ground to a 600 grit finish with SiC paper immediately prior to testing, then degreased in acetone, then ethanol, and dried under flowing nitrogen gas. Coupons were weighed with a precision digital balance to the nearest 0.1 mg, then mounted in PTFE corrosion fixtures with polyethylene screws. Polymers were used for all coupon fixtures to prevent galvanic interactions. The fixtures were in turn placed in polyethylene test chambers as shown in Fig. 1. Fig. 1a and b shows the coupon placement during headspace exposure. All test chamber components were sterilized in an autoclave prior to corrosion tests. Fig. 1c shows the coupon placement during aqueous exposure; three coupons were placed in each test chamber, as indicated. Three chambers were loaded with coupons (3 coupons in each chamber, 9 total) during the headspace tests, and a single chamber (containing 3 coupons) was loaded during aqueous exposure tests. After coupons were secured in each chamber, 225 mL of growth media was poured into the bottom of each headspace chamber. An additional 25 mL of established *A. aceti* culture was pipetted into the growth media solution after lids were secured on chamber tops. The aqueous exposure chamber contained 450 mL of growth media inoculated with 50 mL of *A. aceti* culture to maintain an adequate solution volume-to-surface-area ratio suggested by the standard test method [27].

### 2.4. Sample collection

Acidity and solution optical density (proportional to cell concentration) were monitored periodically through the duration of the test by extracting test solution through a pipette after agitating the tank to ensure even distribution of the cultured cells. Uncertainty in pH measurements was  $\pm 0.03$  pH units (1 s.d.) and optical density uncertainty was  $\pm 1 \times 10^{-3}$  absorbance units for all measurements reported here. Optical density was measured with a UV-VIS spectrometer set at 600 nm wavelength. Growth media solution was replenished every two to three days by replacing the solution volume (typically 10 mL) extracted for pH and optical density measurements.

One coupon was collected from each headspace chamber at time points selected based on pH and absorbance readings (discussed below). The copper coupons were collected at 292 h, 550 h, and 863 h from the time of test initiation and the steel coupons were collected at 355 h, 643 h, and 932 h from the time of test initiation. All three coupons were pulled simultaneously from the aqueous exposure test chamber after 863 h (copper) and 932 h (steel) exposure time. The coupon mass was determined while corrosion product was still intact to determine mass gain due to film formation. Corrosion product was then removed according to

**Table 1**  
Chemical composition limits of 1018 steel and copper alloy 110 (wt.%).

Alloy	Fe	C	Si	Mn	Cu	Pb	Bi	O	S	P
1018	Bal.	0.16	0.15	0.79	–	–	–	–	<0.05	<0.04
110	–	–	–	–	Bal.	<0.005	<0.005	<0.04	–	–

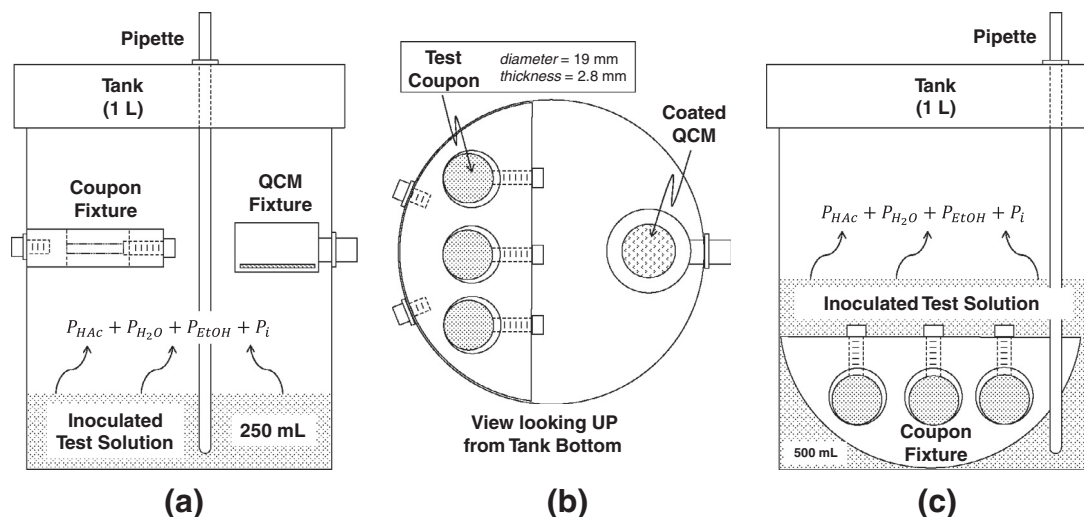


Fig. 1. Corrosion test chambers for headspace exposure testing shown from side view (a) and bottom view (b). Test chamber for aqueous exposure testing is shown in (c).

ASTM G1 and the coupons were weighed again to determine total mass loss. Coupons were dried and stored in a desiccator for metallurgical analysis with standard techniques for optical microscopy and scanning electron microscopy (SEM). The corrosion rate was determined with gravimetric analysis according to ASTM G31 Standard Practice for Laboratory Immersion Corrosion Testing of Metals [27]. Corrosion rates reported here are average values of those determined with three specimens tested at each condition.

### 2.5. Quartz crystal microbalances

Quartz-crystal microbalances (QCMs) were obtained with coatings of 400 nm of iron on a 5 MHz QCM. QCMs were mounted in a crystal holder. The instrument was used to measure the fundamental frequency of the QCM in the headspace over time. This frequency was monitored until failure (due to acid corrosion). The Sauerbrey equation [28] was used to calculate mass of the iron film. This loss of mass over time to failure was used to calculate a corrosion rate.

### 2.6. Coupon characterization

Corrosion product scraped from the coupons was evaluated using thermogravimetric analysis (TGA), X-ray diffraction (XRD), optical microscopy and SEM. Dried corrosion product was ground to a fine powder with a mortar and pestle for both TGA and XRD. TGA samples (approximately 5 mg) were analyzed by heating the samples in alumina crucibles at a rate of  $10\text{ }^{\circ}\text{C min}^{-1}$  to  $1000\text{ }^{\circ}\text{C}$  in a  $20\text{ mL min}^{-1}$  flowing-air environment. Corrosion product powder (approximately 1 mg) was mounted to glass slides by use of double-stick tape for XRD. XRD spectra were obtained by use of a Cu K $\alpha$  source with a monochromator and  $2\theta$  goniometer arrangement. Scans were stepped from  $20^{\circ}$  to  $90^{\circ}$  at a step interval of  $0.04^{\circ}$  and dwell time of 30 s at each interval. SEM imaging and energy-dispersive spectroscopy (EDS) were performed at 10 and 15 kV accelerating voltage. Coupon and QCM surfaces were imaged on a low-power optical microscope at  $7\times$  to  $30\times$  magnification. Localized corrosion was evaluated by measuring pit depths on SEM micrographs with calibrated digital image analysis software following standard techniques for pitting analysis [29].

### 2.7. Calculation of headspace acid concentration

Concentration of acetic acid in the solution and the headspace during corrosion tests were approximated with the solution

acidity, which was determined by submerging a pH probe into pipetted samples. Acetic acid is a weak acid, which does not completely dissociate in water ( $\text{p}K_a = 4.76$ ) or water–ethanol mixtures. Also, growth medium was present; therefore, development of a calibration curve was necessary to determine the relationship between pH and acetic-acid concentration. Reagent-grade acetic acid was mixed at known concentrations into sterile growth-media solution in the presence of 5% ethanol to determine the pH values as shown in Fig. 2a. A linear fit was used to correlate aqueous concentration of acetic acid and the measured pH.

There is proportionality between the acetic acid concentration in the growth media and the concentration of acetic acid in the headspace. Acetic acid is assumed to be a solvent in the growth-media solution, and is assumed to have a concentration above the solution that is dependent on its partial pressure. Acetic acid vapor pressure,  $P_0$ , is dependent on temperature,  $T$ , and obeys Eq. (2) [30,31]:

$$\log P_0 = 4.68206 - \frac{164,254}{-39.764 + T}, \quad (2)$$

where vapor pressure is in bar and temperature in K. We assume that evaporation of acetic acid (HOAc) obeys Raoult's Law [14], where its partial pressure,  $P_{\text{HOAc}}$  is proportional to its mole fraction in solution,  $\chi_{\text{HOAc}}$  according to:

$$P_{\text{HOAc}} = \chi_{\text{HOAc}} \cdot P_0, \quad (3)$$

where vapor pressure,  $P_0$  is described by Eq. (2).

The concentration of acetic acid in the growth media solution is determined with the empirical relationship developed in Fig. 2a, and is described by Eq. (4):

$$\log[\text{HOAc}] = -1.8561 \cdot \text{pH} + 4.9674. \quad (4)$$

As an estimate, we assume that the headspace is a mixture of ideal gases and that the concentration of acetic acid ( $\chi_{\text{HOAc}}$ ) in parts per million by mass is described by Eq. (5):

$$\chi_{\text{HOAc}} = 10^6 \frac{P_{\text{HOAc}} \cdot MW_{\text{HOAc}}}{P_{\text{air}} \cdot MW_{\text{air}}}, \quad (5)$$

where  $P_{\text{air}}$  is 0.867 bar (typical pressure at 1655 m elevation in Boulder, CO) and the molecular weights of acetic acid and air are  $60.05\text{ g mol}^{-1}$  and  $28.966\text{ g mol}^{-1}$ , respectively.

Combining Eqs. (2)–(5) results in a relationship that describes acetic acid concentration in the headspace as a function of both temperature and pH. Fig. 2b shows a plot of the calculated concentration for constant pH values (between 2.5 and 3.6) as a

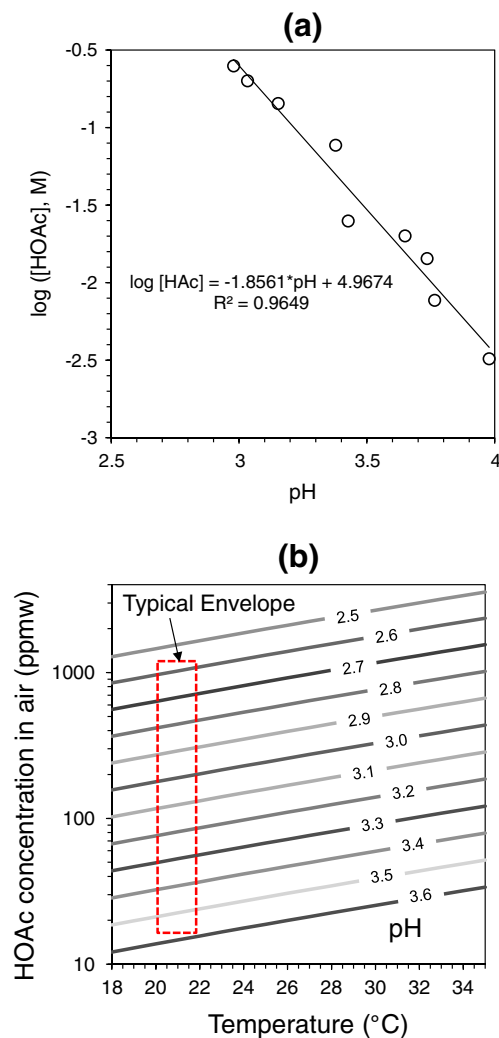


Fig. 2. Acetic acid molar concentration in the growth media as a function of pH (a), and calculated acetic acid vapor concentration in the headspace as a function of solution pH and temperature (b).

function of temperature. The typical concentration envelope is outlined, since lab temperature was maintained between 20 °C and 22 °C during tests (nominal temperature was 21 °C).

### 3. Results and discussion

#### 3.1. Biotic acetic acid production

Growth-media acidity and optical density (proportional to solution absorbance) were used over the duration of the tests, from the time of inoculation, to monitor bacterial growth. Higher solution absorbance and decreased pH correspond to increasing cell concentration (cells mL<sup>-1</sup>). Measured values of solution acidity and optical density in a copper and steel headspace corrosion test were recorded and are shown in Fig. 3. On each figure, solution pH is plotted against the left vertical axis and optical density is plotted against the right vertical axis. Initial acidity (immediately after inoculating the growth media) was typically in the range of 3.2–3.6 pH units, as indicated by the zero-time point. After several days of incubation, bacteria began to multiply according to the exponential increase in the optical-density measurements (note the logarithmic scale on the vertical axes depicting solution absorbance). Multiplication of the culture coincided with an exponential

decay in the solution acidity to final pH values that were typically on the order of 2.6 units. Bacteria reached a steady-state condition, the stationary phase, indicating there are either limited resources (metabolites, etc.) or toxic conditions to preclude further multiplication. The stationary phase occurred at the region where pH no longer changed; however, it is expected that the food source was being consumed at a maximum rate, as *A. aceti* can sustain acetic acid concentrations up to 7% v/v, well above the 0.08% v/v highest measured concentration under the conditions of this test [32]. Arrows along the time-axis of the plots in Fig. 3 indicate the time points at which corrosion coupons were removed from each tank. An attempt was made to remove the first three coupons at the end of the pH decay period to capture effects of transient acidity on corrosion rate. This resulted in slightly different time intervals when removing the copper versus the steel coupons as listed in Section 2.4. However, it is apparent that pH still decreased slightly just after removal of the first coupon, in both examples shown.

Headspace acid concentration was calculated with the procedure described in Section 2.7. Fig. 4 shows the calculated acetic acid concentration in the headspace of the three corrosion chambers during corrosion tests of the steel alloy. The reduction in pH due to microbial metabolism resulted in an exponential increase of acetic acid vapor above the solution that is available to react with alloy surfaces. Note that increasing temperature will have a

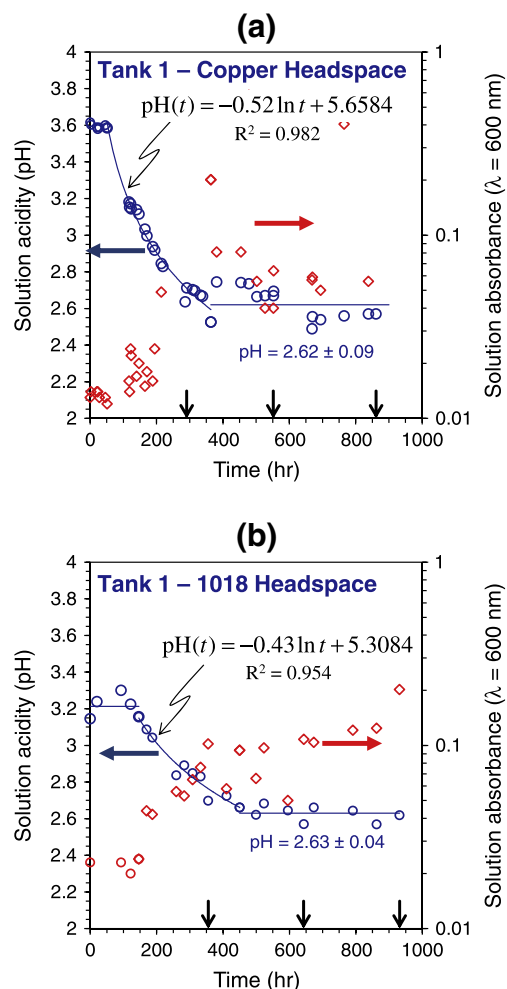


Fig. 3. Relationship between solution acidity (○), solution absorbance (◇), and time after inoculation of growth media for a (a) copper headspace test and (b) a steel headspace test. Arrows normal to the time-axis indicate when corrosion coupons were removed.

significant effect on evaporation of acetic acid (Fig. 2b), in addition to its potential to increase bacteria activity. Therefore, it is expected that higher temperatures would promote significant increases in headspace acetic acid concentration, although not under the relatively isothermal conditions within the test conditions reported here. The chambers were kept at an ambient temperature of  $21 \pm 1$  °C, which was used in Eq. (2).

The headspace acetic acid concentration calculations were performed for the copper corrosion tests (although not shown), and they exhibited similar trends and reproducibility to that of the steel tests. This is not surprising since the same chambers were used for both series of tests. Variability in the headspace composition between the three test chambers used for corrosion testing is demonstrated by the average values and error bars (showing standard deviation) plotted against the secondary vertical axis of Fig. 4. Calculated headspace concentration typically varied 20–30% among the three tanks. This is caused by the variation in pH of the test solution which is used as a primary input for the calculation.

The solution containing immersed copper coupons had variable pH levels within the range of 3.2–3.6 over test duration. These values correspond to acetic acid concentrations of 0.11 M and 0.02 M, respectively according to Eq. (4). The solution containing immersed steel coupons decayed from pH levels of 3.2–2.65 over the duration of the test, corresponding to an acetic acid concentration increase from 0.11 M to 1.39 M.

## 3.2. Gravimetric analyses

### 3.2.1. Headspace coupons

The corrosion rates ( $\text{mm year}^{-1}$ ) of the copper and steel exposed to vapor phase in the headspace were determined with gravimetric analysis and are reported in Fig. 5. Bacteria inoculation was performed at the zero-time point. Since three test chambers were inoculated simultaneously during testing of both alloys, each data point represents the average corrosion rate of three coupons (one pulled from each of the three test chambers) at each time point. Standard deviations of each corrosion rate data-set are indicated with error bars. The corrosion rate of the copper, which initially increased rapidly, reached a maximum value of approximately  $0.06 \text{ mm year}^{-1}$  half way through the exposure period (Fig. 5a). Corrosion rates of the steel, which were an order of magnitude higher than those determined for copper, also increased rapidly near the beginning of the test, compared to the end, where rates exceeded  $1 \text{ mm year}^{-1}$  (Fig. 5b).

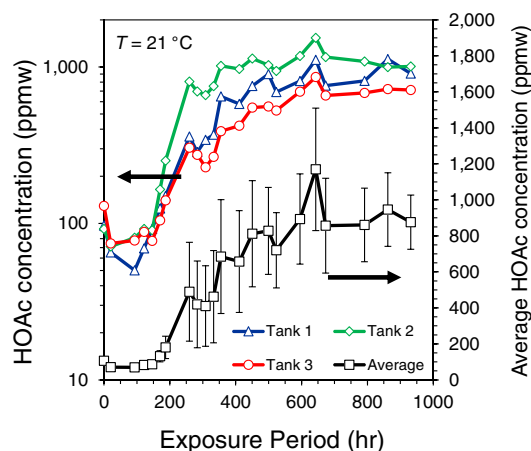


Fig. 4. Calculated acetic acid concentration as a function of time in the test chamber headspace during steel coupon exposure.

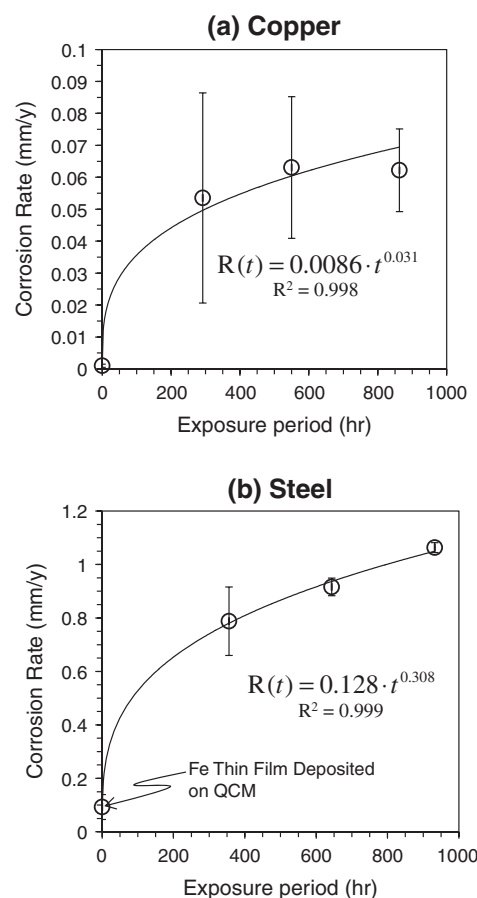


Fig. 5. Relationship between exposure period in the headspace environment and the corrosion rates of (a) copper and (b) steel determined with the gravimetric and QCM methods.

Two of the test chambers produced similar corrosion-rate data, while the third chamber produced significantly lower corrosion rates during the first half of the copper corrosion tests. This resulted in the large standard deviation in measured copper corrosion rates shown in Fig. 5a. Variability in headspace concentration between the tanks was demonstrated in Fig. 4 with calculations. The particular chamber that produced lower corrosion had fewer portals for sampling and pipetting, which potentially reduced oxygen concentrations in that particular tank and could potentially have led to slower bacteria metabolism of the aerobic *A. aceti*. The particular chamber also exhibited lower optical density measurements in comparison to the other two tanks resulting in slightly lower acidity in the growth-media solution. Note that when corrosion rate was higher in the case of the carbon steel, the sensitivity to this variability in metabolism was significantly reduced.

The plots of headspace corrosion rate show a parabolic relationship between corrosion rate and exposure period, which is a characteristic typically observed in atmospheric corrosion of carbon steels and copper alloys [33]. An empirical relationship between the corrosion rate,  $R$ , initial corrosion rate,  $A$ , and exposure time,  $t$  is given by Eq. (6):

$$R = A \cdot t^n, \quad (6)$$

where the exponent  $n$  describes the ability of corrosion products formed on the alloy surface to protect against corrosion. This model has been fitted to the experimental data as indicated in Fig. 5, where the fitted equations show a high coefficient of determination ( $R^2$ ) in both cases, indicating good fit. It has been suggested [33] that when the  $n$ -values are below 0.6, the corrosion product possesses

protective ability, whereas as  $n$ -values approach unity, the film provides little protective ability. The fitted models in Fig. 5 demonstrated that the protectiveness of the copper corrosion product ( $n = 0.031$ ) is an order of magnitude higher than that formed on the surface of the steel ( $n = 0.308$ ), which is expected, given the higher corrosion rates produced on the steel. This has important practical implications regarding corrosion of sump components observed in field inspections. Removal of corrosion product would likely be detrimental to corrosion rate even though its visual appearance may be quite undesirable to inspectors or operators.

Corrosion rates of copper [14] and steel [16] are both dependent on abiotic acetic-acid content in the vapor phase. Copper corrosion rate, as a function of acetic-acid vapor content, increases sharply with concentration until the vapor content reaches saturation at approximately 150 ppm; further increases are not appreciable above ~200 ppm [14]. Bacteria within the test chambers here likely produce acetic-acid vapor concentrations (~900 ppm at pH = 2.6) well above the levels previously demonstrated to achieve the saturated corrosion rates of copper, at least after the initial decay in pH. Steel corrosion rate depends strongly on acetic-acid content, even at concentrations up to 300 ppm, and exhibits no such saturated corrosion rate at a given concentration of acetic acid [16] as seen in studies of copper corrosion. Since corrosion rate has shown dependence on acid concentration, future parametric studies evaluating headspace concentration and temperature would enable more robust corrosion models of the alloys studied here.

### 3.2.2. Quartz crystal microbalance

Quartz-crystal microbalances were used to establish corrosion rates on a shorter time scale than those used in the coupon test, i.e., they were used to evaluate initial transient mass change. These low initial corrosion rates are indicative of exposure to the 8 h culture, which has been grown in an ethanol-containing environment and already contains dilute acetic acid. An iron-coated QCM was suspended in the headspace at approximately the same height as the coupons. Corrosion of the iron film was monitored as a change in frequency. After approximately 8 h, the 400 nm iron film was degraded and signal quality was diminished. A corrosion rate was determined for these first 8 h by calculating the change in mass from the change in frequency,  $f$  using the Sauerbrey equation (briefly,  $\Delta f = \text{constant} * \Delta \text{mass}$ ) for the given mass of iron over the active area of the QCM. The corrosion rate ( $0.092 \text{ mm year}^{-1}$ ) was plotted in Fig. 5b and used in the data fitting for steel as an initial corrosion rate.

### 3.2.3. Immersed coupons

Steel and copper coupons were submerged into freshly inoculated ethanol growth media in a fourth tank. Gravimetric analysis revealed corrosion rates of  $0.051 \pm 0.010 \text{ mm year}^{-1}$  (863 h exposure) and  $0.061 \pm 0.003 \text{ mm year}^{-1}$  (932 h exposure) on the copper and steel, respectively. The corrosion rate of the copper immersed in solution is on the order of that observed in the headspace, whereas the corrosion rate of steel was significantly lower when immersed as compared to vapor-phase exposure. Given the similarity in corrosion rates of copper exposed to aqueous and vapor phases, the vapor phase corrosion is controlled by continuous layers of condensed acetic acid available for surface reaction.

Carbon-steel corrosion rates were determined in abiotic acetic-acid solutions with concentrations similar to those studied here [34]. The steel corrosion rates previously reported (approximately  $1.2\text{--}1.8 \text{ mm year}^{-1}$  [34]) are much higher than observed here when steel was immersed in the biotic acetic acid. Such low corrosion rates reported in the current work are indeed surprising since the solution pH reaches levels of approximately 2.65. In general, corrosion rate of steel increases significantly below pH levels of

approximately 4 under aerated conditions, due to availability of sufficient  $\text{H}^+$  for reduction by [35]:



or by



in the presence of dissolved oxygen.

During post-test coupon analysis in this study, *A. aceti* biofilms were observed on the surface of carbon steel exposed to the aqueous environment. It is likely that anoxic conditions were produced at the interface of the biofilm and the steel coupon as the *Acetobacter* colony thickened, precluding Reaction (8). Low corrosion rates of steel observed here could thus likely be attributed to the protective nature of the biofilm in the inoculated growth media as a result of aerobic consumption of molecular oxygen [36] and its capacity to serve as a corrosion reactant at the steel surface. Alternatively, the biofilm coverage may preclude the adsorption of acetate ions on the steel surface, which is a necessary step in the formation of cathodic hydrogen for Reaction (7) to commence [34]. Test media used for maintaining a bacteria culture can influence microbial binding and may accelerate corrosion reactions [37]. A combination of all of these potential contributions is likely.

Copper, having an antimicrobial effect [38], did not exhibit the same protective biofilm observed visually on the steel coupons. In the chamber used for the copper immersion tests, the microbe-containing solution had a distinct blue color (due presumably to formation of copper acetate), and a biofilm suspended in the solution had distinct morphology. During steel corrosion testing, *A. aceti* formed clumpy films within the solution, but formed a thin surface film on the water–air interface in the chamber containing copper coupons. No significant clumps were observed in the solution and no biofilm was observed on the surfaces of the copper coupons.

### 3.3. Corrosion product analyses

The typical appearance of the copper and steel coupons after removal from the headspace chambers are shown in Fig. 6a and b, respectively. Note the different exposure times. Blue corrosion product spread over the entire surface of the copper with increasing exposure time. The crystallite morphology of this product matched that seen on copper tubing contained on sump components in underground storage tanks reported elsewhere [7]. Top surfaces of the copper coupons appeared to have greater surface coverage of corrosion product and it was noted that during testing, greater condensation appeared on the top surfaces also, since radial direction of the coupons was oriented parallel to the inoculated solution. Such condensation would lead to higher acetate concentrations on the top surface of the coupons, resulting in greater surface area coverage of reactant. The copper corrosion product was quite hard compared to the steel corrosion product, which flaked easily from the coupons. Steel corrosion product was greater in thickness than the coupon at the later time points and also reproduced the nature of the corrosion seen on submersible turbine-pump cases in the underground storage-tank sumps [7].

Corrosion products were removed from the copper coupons and analyzed by TGA and XRD to determine phase content. Copper corrosion products demonstrated three major oxidation temperatures by TGA (Fig. 7a), representative of copper acetate transitions previously reported [39]. The first oxidation step, at  $139.3 \pm 1.9 \text{ }^\circ\text{C}$  (2 s.d.), was a mass loss attributed to the dehydration of copper acetate and formation of copper acetate peroxides. The second transition, at  $270.6 \pm 0.12 \text{ }^\circ\text{C}$  (2 s.d.), was attributed to the further

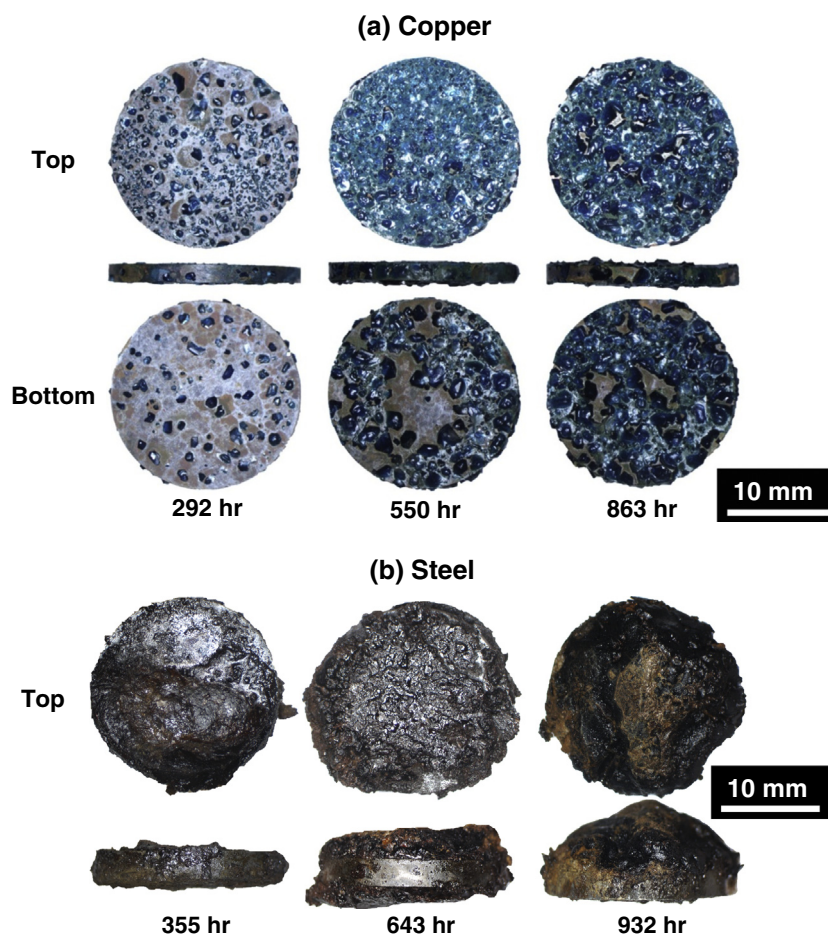
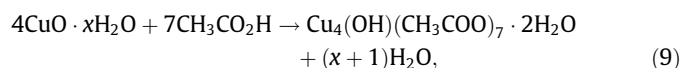
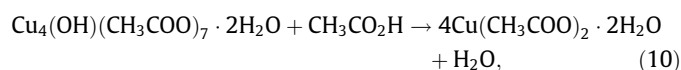


Fig. 6. Optical micrographs of (a) copper and (b) steel after exposure to headspace environment for indicated exposure periods.

oxidation of the copper acetate into smaller decomposition products. The final transition, at  $283.3 \pm 0.12$  °C (2 s.d.), is the transition observed of the copper products remaining after step 2 into cupric oxide. The small mass increase above approximately 290 °C is attributed to oxidation of cupric oxide. XRD results from two copper corrosion product samples are shown in Fig. 7b. Comparing to literature values, the majority of the products can be identified as copper acetate dihydrate,  $\text{Cu}(\text{CH}_3\text{COO})_2 \cdot 2\text{H}_2\text{O}$ , with some cuprite ( $\text{Cu}_2\text{O}$ ) products also represented [14]. In the presence of acetic acid,  $\text{CuO}$  is converted to copper hydroxide acetate according to the reaction:



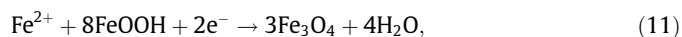
and is then further converted to copper(II) acetate in the presence of high levels of acetic acid by:



which matches corrosion products previously reported in the literature.

Corrosion products from the steel coupons were also analyzed with TGA (Fig. 7c) and XRD (Fig. 7d). The major expected product is an iron oxide-hydroxide, most likely the  $\alpha$ -FeOOH product. A small mass loss is observed in the thermogram at  $127.6 \pm 5.5$  °C (2 s.d.), followed by a broad transition centered around  $227.8 \pm 8.8$  °C (2 s.d.) and sharper transition at  $279.5 \pm 3.5$  °C (2 s.d.). The first mass loss was attributed to the loss of absorbed

water in the sample. The broad transition is most likely the dehydration/dehydroxylation of surface Fe (oxo)hydroxo-functional groups, which have been well characterized [40]. The major mass loss at 275.9 °C was attributed to the conversion of iron(II) hydroxide to iron(III) oxide. Analysis of the XRD product further supports that the corrosion occurred by typical atmospheric-rusting kinetics models to yield FeOOH as the major product [16,41]. Briefly, the reaction can be described as:



followed by additional conversion of the magnetite to FeOOH products through the following reaction [16]:



XRD confirmed the presence of FeOOH products when compared to literature values [42], and infrared spectroscopy (not shown) confirmed that no iron acetate products formed on the steel.

Protective ability of corrosion product was related empirically to corrosion rate based on the constant  $n$  in Eq. (6). Steel corrosion product loosely adhered to the coupon surfaces after headspace exposure, flaking easily with any agitation or physical contact. The FeOOH can remain protective in moist atmospheres free of contamination by other compounds [43]; however, it was quite porous, unlike the copper acetate corrosion product, which formed tightly adhered crystals described by the patination mechanism in Ref. [14]. These crystals evidently formed a more protective barrier once continuous coating of the copper surface is complete, since the coefficient  $n$  is an order of magnitude lower than that of the

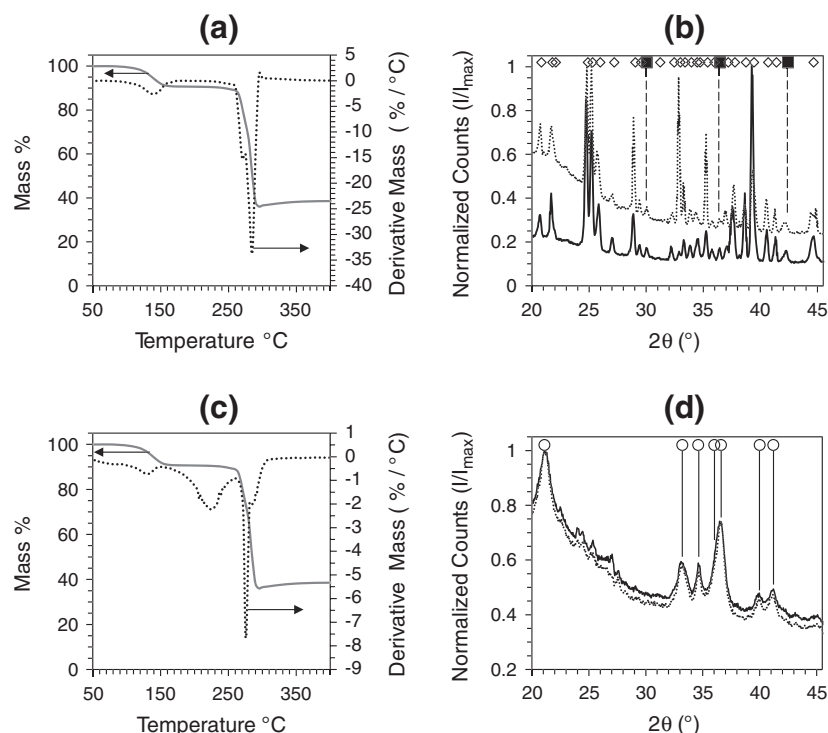


**Fig. 7.** Corrosion product analysis. (a) TGA of copper corrosion product (solid line) and its derivative with respect to temperature (dashed line); (b) XRD data from two copper corrosion product samples. Diamonds indicate Cu(CH<sub>3</sub>COO)<sub>2</sub>·2H<sub>2</sub>O and squares indicate Cu<sub>2</sub>O; (c) TGA of steel corrosion product (solid line) and its derivative with respect to temperature (dashed line) also shown; (d) XRD data from two steel corrosion product sample. Circles indicate FeOOH.

steel corrosion product. Corrosion mechanisms in the headspace tests conducted here do not vary significantly from similar, but abiotic conditions reported in the literature.

### 3.4. Materials damage morphology

#### 3.4.1. Copper corrosion

Previous studies [14,19] reporting on acetic-acid vapor corrosion of copper focused on evaluating the corrosion layers built up on the surface, and did not report the metallurgical damage observed here in the underlying metal once corrosion product was removed. Metallurgical damage should be characterized, as it often affects mechanical performance of mechanically stressed components, and could potentially influence the reliability of copper components in the sump environments. Corrosion pits act as stress concentrators, and in highly stressed parts, stress-corrosion cracks (SCC) often initiate at such sites. This is of concern in the heavily cold-worked copper tubing, where residual stresses (which also influence corrosion) are quite high due to the tube-forming processes, since the bursting of such a component could lead to leakage of fuels into the environment. Intergranular corrosion may also lead to SCC in stressed materials as formation of Cu<sub>2</sub>O film along grain boundaries induces SCC in pure copper material exposed to cupric-acetate solution [44]. Cu<sub>2</sub>O was observed in the TGA and XRD analyses presented above suggesting that SCC would be highly likely in the UST copper tubing sump components containing significant concentrations of biotically produced acetic acid.

The corroded surfaces of coupons exposed to headspace vapor phase for 863 h were examined by SEM after removal of the crystalline copper-acetate corrosion product (Fig. 8a). Pitting attack on the surface of the copper was evident. Many small pits were noted, and these often coalesced into larger pits like that shown in the figure. General corrosive attack was also noted, as the grinding marks

associated with the coupon preparation procedure had been corroded away during the exposure. Contrary to the coupons exposed to headspace, a mixed-mode general attack and intergranular corrosion were observed along the copper grain boundaries of coupons immersed in the inoculated solution, as shown in Fig. 8b. The corroded surface clearly shows the faceted features associated with the copper grain boundaries.

The copper coupons were cross-sectioned and analyzed with SEM to evaluate the depth of pitting attack and intergranular attack modes. Corrosion pits produced during headspace exposure (Fig. 8c and d) penetrated as deep as 85 μm into the coupon over the longest test duration (863 h), although most of the pits were less than approximately 25 μm in depth. Intergranular corrosion associated with aqueous exposure to the inoculated growth media is seen in Fig. 8e. Note the intersection of grain boundaries with the surface of the coupon and the corresponding corrosive attack at those locations. Similar to the pit depths, the depths of the intergranular attack were on the order of 38 μm after the longest exposure times. Maximum observed attack rates of pitting in the headspace and intergranular attack while immersed in inoculated solution were 2.4 μm day<sup>-1</sup> (0.876 mm year<sup>-1</sup>) and 1.1 μm day<sup>-1</sup> (0.402 mm year<sup>-1</sup>), respectively. These numbers indicate that both forms of localized corrosion occur at rates that are an order of magnitude higher than the rates of general corrosion reported in Fig. 5. These measurements of localized corrosion are based on a limited sample set, since only one cross-sectional plane of one coupon was analyzed with SEM for each test condition. Therefore, localized attack rates determined here are conservative and could be higher.

The copper alloy tested here was a high-purity grade. However, some oxide particles were observed in the microstructure (Fig. 8e), which was not surprising since there is some allowance for oxygen in this particular alloy, as shown in Table 1. XRD revealed that cuprite was a stable phase in the coupons exposed to the headspace. One mechanism for copper pitting in freshwater systems

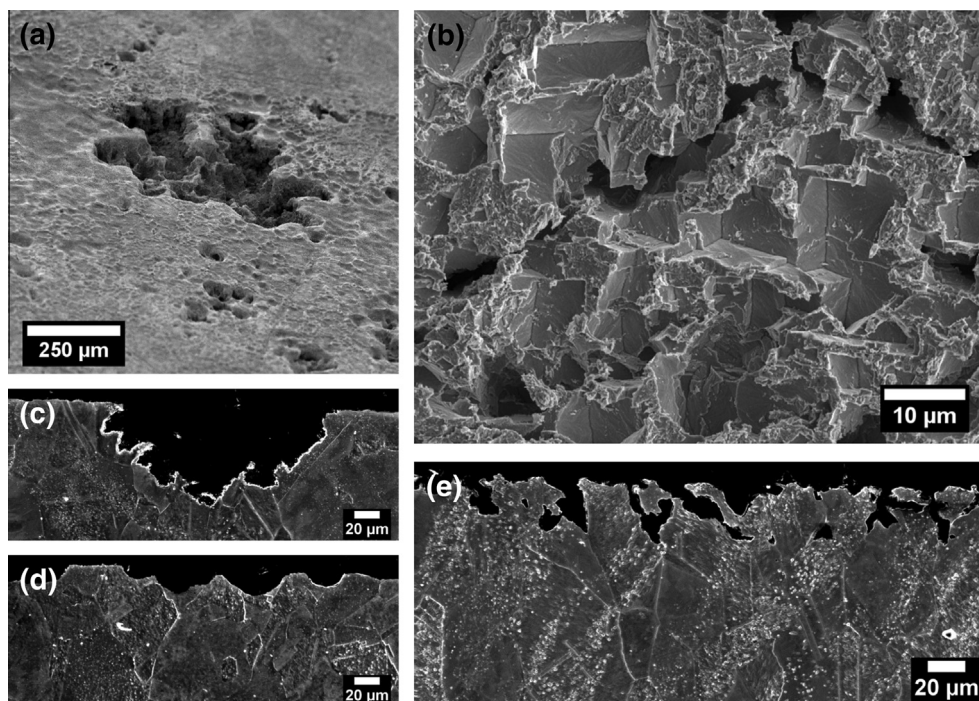


**Fig. 8.** Secondary electron micrographs of copper showing (a) coupon surface after headspace exposure and removal of corrosion product, (b) coupon surface after immersion in inoculated solution, (c and d) cross-section of coupon showing pitting after headspace exposure, (e) cross-section of coupon showing intergranular attack.

suggests that pits initiate when surface nodules of hydrated copper salts create a pinhole in the underlying cuprite layer [43]. The XRD supports this mechanism as both cuprite and copper salts are formed on the coupon surfaces. Copper surfaces exposing any such oxides would produce a galvanic cell between the oxide and the metal itself, creating large polarizations between oxide and metal, and would be the likely metallurgical feature for initiation of the corrosion pits during vapor exposure. The intergranular attack mode produced during immersion in the inoculated solution is clearly distinct from the pitting, and may be related to segregation of any impurity elements (shown in Table 1) to the grain boundaries. The chemical analysis techniques used herein were unable to identify any such segregation, since the levels of impurities are likely in the ppm range.

#### 3.4.2. Steel corrosion

The steel corrosion damage after headspace exposure consisted of both general attack (since any evidence of coupon preparation grinding was removed) and pitting. Fig. 9a shows extensive pitting on a steel coupon after exposure to headspace for 932 h. Close observation of the pit cores is presented in Fig. 9b along with qualitative EDS analyses of the regions indicated on the image. Quantitative analysis was not possible due to lack of appropriate standards for steel containing high Mn and S. The pit cores almost always contained evidence of metallurgical inclusions consisting of manganese and sulfur, which is likely in the form of MnS. The 1018 steel rod used for corrosion testing was rolled; thus, the inclusions would have the tendency to elongate along the axis of rolling process. These elongated inclusions result in deep penetration of pitting into the coupons as shown in Fig. 9c, which is a cross-section of the coupon shown in Fig. 9a. Rather than the typical pitting mechanism where chloride is involved, a galvanic potential is possible between the MnS and the surrounding steel matrix, promoting iron dissolution adjacent to the inclusion. This is localized in the particular material tested, as the pits penetrated deep into the steel surface. Pockets of corrosion were observed beneath the

pits in many cases, and as these pockets linked together, pits grew to depths that reach well over 0.5 mm during the exposure periods tested here. Fig. 9d reveals the elongated MnS inclusions located at the base of the pit shown in Fig. 9c and corresponding qualitative chemical analysis.

While the average corrosion rate of steel coupons exposed to the inoculated growth media was actually quite low, extensive metallurgical damage occurred as evident upon close inspection of the coupons following testing. Fig. 10a shows the surface of the coupon after exposure, which revealed small pits across the specimen. Some preferential attack was observed at the interface between the ferrite and cementite ( $\text{Fe}_3\text{C}$ ) phases, although this was quite minor in nature compared to the pitting attack. The coupon in Fig. 10a was cross-sectioned and reexamined (Fig. 10b). The deep pitting attack along MnS inclusions was observed again, and was similar to that shown in the headspace, although narrower in width. It is noteworthy that the attachment of *Acetobacter* sp. appear to provide extensive protection from general corrosion when compared to acetic acid corrosion rates of steel reported elsewhere [34]; however, they have little ability to protect against pitting and localized attack on MnS, and can actually promote the formation of differential aeration cells that exacerbate pitting of carbon steel [45]. In fact, pitting depths were greater in the immersed condition. Therefore, attempting to control corrosion by encouraging an *Acetobacter* biofilm could be impractical.

Maximum observed attack rates of pitting in the headspace and while the coupon was immersed in inoculated solution were  $12.9 \mu\text{m day}^{-1}$  ( $4.7 \text{ mm year}^{-1}$ ) and  $7.8 \mu\text{m day}^{-1}$  ( $2.85 \text{ mm year}^{-1}$ ), respectively. The elongated morphology and orientation of the MnS inclusions played a significant role in governing this extensive pitting damage in the steel alloy tested here. Metallurgical processing with other techniques, such as steel- or iron-casting used in sump-pump case production, could promote inclusions with a morphological nature different from those observed here. MnS is present in most steel alloys, and such

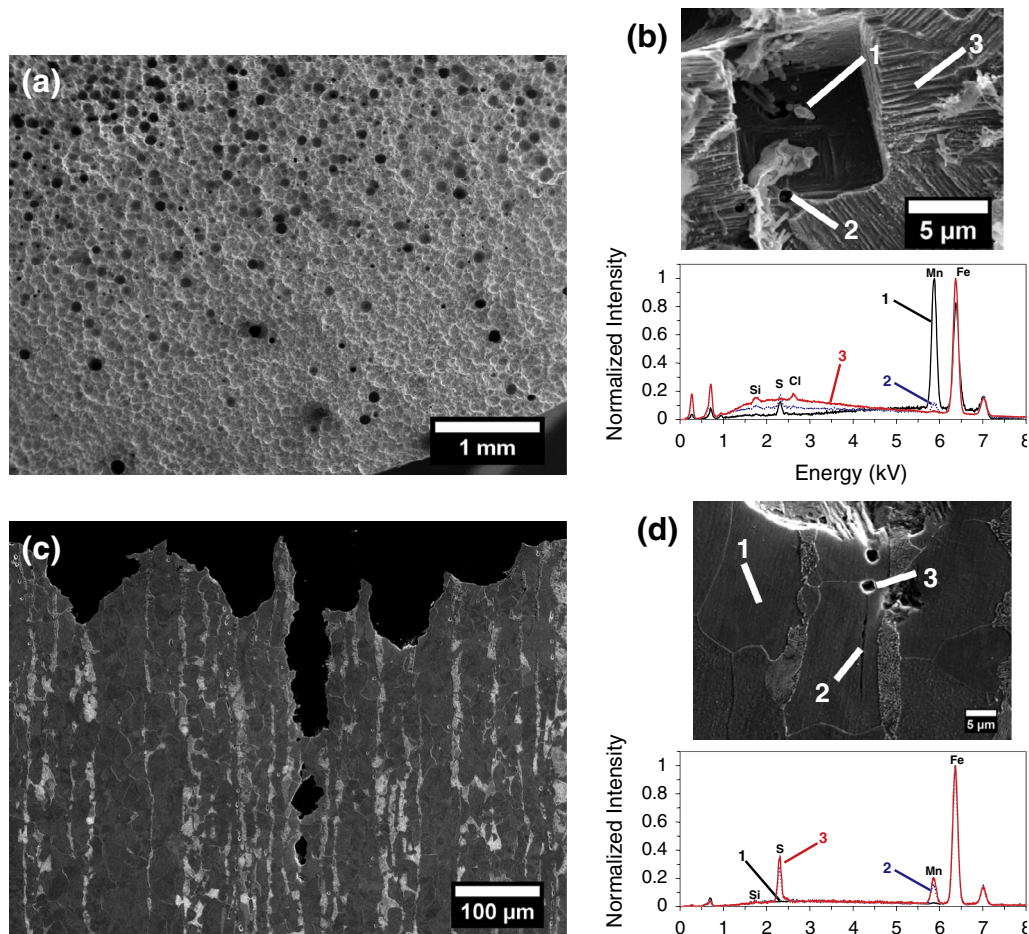


**Fig. 9.** Secondary electron micrographs of steel showing (a) coupon surface after headspace exposure and removal of corrosion product, (b) analysis of MnS particles inside a corrosion pit, (c) cross-section of coupon showing pitting after headspace exposure, (d) close-up of inset in (c) and corresponding analysis of MnS particles at pit base.

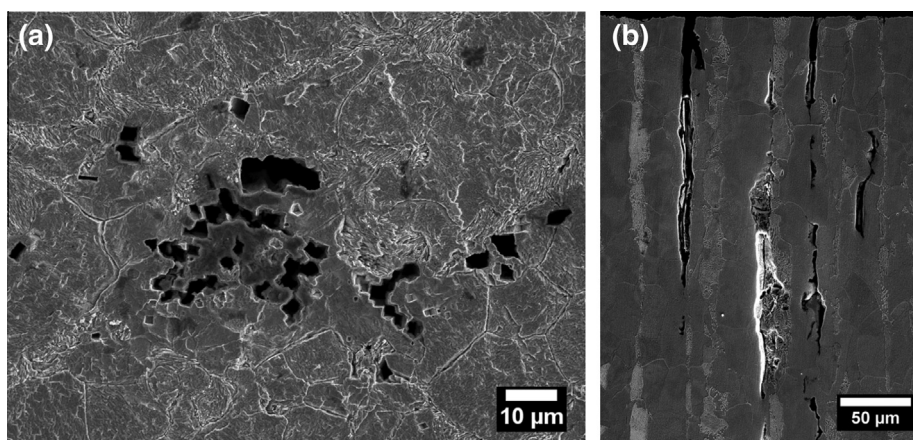


**Fig. 10.** Secondary electron micrographs of steel showing (a) coupon surface after immersion in inoculated solution and (b) cross-section of coupon showing pitting penetration along MnS inclusions.

attack is expected along those inclusions. Steels of very low sulfur content may perform much better with respect to corrosion resistance in *Acetobacter*-containing environments, since the lesser inclusion distribution would drastically reduce the ability for localized corrosion to occur.

A summary of the localized and general corrosion rates for each material and environment combination is shown in Table 2. The measured attack rates were used to calculate the Pitting Factor,  $PF$  (where  $PF = \text{deepest metal penetration} / \text{average metal}$

penetration) to provide a tendency towards localized corrosive penetration. A pitting factor of unity represents uniform corrosion, whereas a pitting factor greater than unity represents a tendency towards localized corrosion. The  $PF$  analyses reveals that the steel exposed to the headspace vapor phase had a much lower tendency towards pitting than during aqueous phase exposure. The copper has a tendency towards localized attack in both environments although that tendency appears to be stronger in the headspace vapor phase.

**Table 2**

Summary of localized and general corrosion rates, and calculated pitting factors for copper and steel exposed to vapor phase and aqueous phase.

Exposure type	Copper alloy 110			1018 steel		
	Localized attack rate (mm year <sup>-1</sup> )	General corrosion rate (mm year <sup>-1</sup> )	Pitting factor	Localized attack rate (mm year <sup>-1</sup> )	General corrosion rate (mm year <sup>-1</sup> )	Pitting factor
Vapor phase	0.876	0.060	14.6	2.85	1.10	2.59
Aqueous phase	0.402	0.051	7.88	4.70	0.061	77.0

### 3.5. Relevance to UST sump environments

Several mechanical components in UST systems utilize copper alloys, and many components utilize various steel materials in their manufacture. We have demonstrated that the corrosion rates of copper and low-carbon steel subjected to biotic acetic-acid vapor can experience moderate to high rates of general corrosion and very high rates of localized attack. This plausibly suggests that the mechanical components in the UST systems can experience rapid degradation. Typical industrial-grade copper tubing, for example, has wall thickness between 1.24 mm and 1.65 mm. Given the high rates of localized corrosion we observe after metallurgical evaluation of the coupon cross-sections (0.402–0.876 mm year<sup>-1</sup>), copper tubing of 1.65 mm thickness could perforate quite rapidly under constant exposure to acetic acid. Steel components such as the sump cases have thick walls and would take a considerable exposure period to corrode through the thickness, even at the highest pitting rates of 4.7 mm year<sup>-1</sup>. However, there are many other steel components, including valves and leak detectors, which could fail, potentially causing ground-water contamination. It is likely that with daily and seasonal temperature swings (which could influence the evaporation and condensation of acetic acid) and intermittent availability of ethanol as a carbon source, the actual sump environments would experience more unpredictable corrosion than the models presented here tend to suggest. Standard test methods for evaluating such biotic behavior are not currently available, and this work suggests more research is needed to further develop such methods, which could have broader application in evaluating MIC issues. The data presented are useful for suggesting inspection intervals of UST components and the test protocol reported here has application in evaluating alloy compatibility as well as coating and biocide effectiveness. Volatile corrosion inhibitors (VCI) may provide some beneficial effect in reducing acetic acid headspace corrosion. The VCI dicyclohexylamine nitrite has been shown to be somewhat effective in reducing corrosion rate of steel exposed to acetic-acid vapor, although the efficacy was largely dependent on the humidity level, and benzotriazole is a good VCI for copper and its alloys [16]. Agar-agar and Furfural provide satisfactory protection, and Pyrogallol provides good protection to copper in 0.2 M and 0.5 M acetic acids [46]. Additional testing should, for example, evaluate the efficacy of corrosion inhibitors in the headspace environment.

### 4. Conclusions

We have developed a test method and test chamber to evaluate metal corrosion during exposure to organic acids. The test was used to simulate the environments of an underground storage-tank sump pump contaminated with ethanol fuel and *Acetobacter* sp. From this test, the following conclusions can be made:

1. *A. acetii* sampled from an ethanol fuel production stream and grown in an ethanol-containing environment produced acetic acid, which vaporized and resulted in extensive general and localized corrosion of copper and steel in the headspace above the inoculated aqueous-ethanol solution.
2. General corrosion rates were determined after headspace exposure, where steel corrodes an order of magnitude faster than copper. The lower corrosion rate of the copper was a result of the greater protectiveness of the corrosion product as described by an empirical atmospheric corrosion-rate model. General corrosion rates of each material exposed to the simulated UST conditions are ranked as follows in order of increasing magnitude: Copper-aqueous (0.05 mm year<sup>-1</sup>) < Steel-aqueous (0.06 mm year<sup>-1</sup>) < Copper-headspace (0.06 mm year<sup>-1</sup>) < Steel-headspace (>1 mm year<sup>-1</sup>).
3. Extensive localized corrosion was observed on both materials after headspace exposure and direct exposure to inoculated aqueous-ethanol solution. Pitting along MnS inclusions was predominant in the steel exposed to both conditions, whereas the copper exhibited pitting during headspace exposure and intergranular attack when immersed in solution. Pitting along MnS inclusions is indicative of galvanic attack at the inclusion/steel interface.
4. The rates of localized attack were an order of magnitude greater than the general corrosion rates. For copper, these rates were 2.4 μm day<sup>-1</sup> (0.876 mm year<sup>-1</sup>) and 1.1 μm day<sup>-1</sup> (0.402 mm year<sup>-1</sup>) for headspace and intergranular attack while immersed in inoculated solution, respectively. Maximum observed attack rates of pitting in the headspace and while immersed in inoculated solution were 12.9 μm day<sup>-1</sup> (4.7 mm year<sup>-1</sup>) and 7.8 μm day<sup>-1</sup> (2.85 mm year<sup>-1</sup>), respectively for steel. This indicates that once an attack begins in these systems, the damage can occur at significantly higher rates than might be predicted with a general corrosion-rate model.
5. The rapid corrosion of UST sump pumps by *A. acetii* microbes is plausible, based on corrosion damage and corrosion rates observed here. Further investigation of this particular system could indicate the propensity of ethanol-containing fuel infrastructure to accelerated corrosion rates. The test chamber developed here could be utilized to investigate mitigation strategies to prevent incidents or environmental releases of fuels caused by microbiological corrosion.

### Acknowledgements

We acknowledge the technical assistance of (NIST) Justin M. Shaw for XRD experiments, Kenneth Talley and J. David McColskey for test chamber development, and (Colorado School of Mines) Chase Williamson and John Spear for providing bacteria cultures.

### References

- [1] International Energy Outlook 2010, U.S. Energy Information Administration, Washington, DC, 2010.
- [2] Building Bridges to a More Sustainable Future, 2011 Ethanol Industry Outlook, Renewable Fuels Association, Washington, DC, 2011.
- [3] B. Singh, J. Korstad, Y.C. Sharma, A critical review on corrosion of compression ignition (CI) engine parts by biodiesel and biodiesel blends and its inhibition, *Renew. Sustain. Energy Rev.* 16 (2012) 3401–3408.
- [4] W. Wang, P.E. Jenkins, Z.Y. Ren, Electrochemical corrosion of carbon steel exposed to biodiesel/simulated seawater mixture, *Corros. Sci.* 57 (2012) 215–219.

- [5] S. Pollock, Accelerated corrosion of UST equipment (an ethanol hangover), in: 23rd National Tank Conference, 2012.
- [6] Corrosion in Systems Storing and Dispensing Ultra Low Sulfur Diesel (ULSD), Hypotheses Investigation, Battelle Memorial Institute, Columbus, OH, 2012.
- [7] J. Wilson, C. Adair, J. Skender, A. Barbery, L. Thompson, E. Fowler, R. Strauss, K. West, J. Hickey, R. Hansen, E. French, J. Owens, B. Kowalski, E. Humlie, B. Jergenson, Corrosion in STP sumps: what causes it and what can be done about it?, *Petrol Equip. Inst. J.* 7 (2013) 26–34.
- [8] E.C. Hill, G.C. Hill, Microbial contamination and associated corrosion in fuels, during storage, distribution and use, in: V. Agarwala, F. Bellucci, M. Montuori, J. Lppolito (Eds.), *Corrosion in the Military*, Trans Tech Publications Ltd., Stafa-Zurich, 2008, pp. 257–268.
- [9] C.C. Gaylarde, F.M. Bento, J. Kelley, Microbial contamination of stored hydrocarbon fuels and its control, *Rev. Microbiol.* 30 (1999) 1–10.
- [10] L. Jain, C. Williamson, S.M. Bhole, R. Bhole, J.R. Spear, B. Mishra, D.L. Olson, R. Kane, Microbiological and electrochemical evaluation of corrosion and microbiologically influenced corrosion of steel in ethanol fuel environments, in: NACE/I0, NACE International, San Antonio, TX, 2010.
- [11] B.J. Little, J.S. Lee, *Microbiologically Influenced Corrosion*, John Wiley & Sons, New Jersey, 2007.
- [12] D.H. Pope, D. Zintel, A.K. Kuruvilla, O.W. Siebert, Organic acid corrosion of carbon steel: a mechanism of microbiologically influenced corrosion, *Corrosion* 88 (1988) 79.
- [13] L.T. Gibson, C.M. Watt, Acetic and formic acids emitted from wood samples and their effect on selected materials in museum environments, *Corros. Sci.* 52 (2010) 172–178.
- [14] A. Lopez-Delgado, E. Cano, J.M. Bastidas, F.A. Lopez, A laboratory study of the effect of acetic acid vapor on atmospheric copper corrosion, *J. Electrochem. Soc.* 145 (1998) 4140–4147.
- [15] S. Nestic, Key issues related to modelling of internal corrosion of oil and gas pipelines – a review, *Corros. Sci.* 49 (2007) 4308–4338.
- [16] J.M. Bastidas, E.M. Mora, A laboratory study of mild steel vapour phase corrosion and its inhibition by dicyclohexylamine nitrite, *Can. Metall. Quart.* 37 (1998) 57–65.
- [17] S.K. Singh, A.K. Mukherjee, Kinetics of mild steel corrosion in aqueous acetic acid solutions, *J. Mater. Sci. Technol.* 26 (2010) 264–269.
- [18] V.B. Singh, R.N. Singh, Corrosion and inhibition studies of copper in aqueous solutions of formic acid and acetic acid, *Corros. Sci.* 37 (1995) 1399–1410.
- [19] E. Cano, J.M. Bastidas, J.L. Polo, N. Mora, Study of the effect of acetic acid vapor on copper corrosion at 40 and 80% relative humidity, *J. Electrochem. Soc.* 148 (2001) B431–B437.
- [20] M.E. Rauch, H.W. Graef, S.M. Rozenzhak, S.E. Jones, C.A. Bleckmann, R.L. Kruger, R.R. Naik, M.O. Stone, Characterization of microbial contamination in United States Air Force aviation fuel tanks, *J. Ind. Microbiol. Biotechnol.* 33 (2006) 29–36.
- [21] N. Yemashova, V. Murygina, D. Zhukov, A. Zakharyantz, M. Gladchenko, V. Appanna, S. Kalyuzhnyi, Biodeterioration of crude oil and oil derived products: a review, *Rev. Environ. Sci. Biotechnol.* 6 (2007) 315–337.
- [22] ASTM A108-13 Standard Specification for Steel Bar, Carbon and Alloy, Cold-Finished, ASTM International, West Conshohocken, PA, 2013.
- [23] ASTM B187/B187M-11 Standard Specification for Copper, Bus Bar, Rod, and Shapes and General Purpose Rod, Bar, and Shapes, ASTM International, West Conshohocken, PA, 2011.
- [24] C. Williamson, *An Investigation of Microbial Diversity and Microbiologically Influenced Corrosion in Automotive Fuel Environments*, Dept. of Environmental Science & Engineering, Colorado School of Mines, Golden, CO, 2013.
- [25] P. Lisdiyanti, K. Katsura, W. Potacharoen, R.R. Navarro, Y. Yamada, T. Uchimura, K. Komagata, Diversity of acetic acid bacteria in Indonesia, Thailand, and the Philippines, *Microbiol. Cult. Collect.* 19 (2003) 91–99.
- [26] ASTM G1-03(2011) Standard Practice for Preparing, Cleaning, and Evaluating Corrosion Test Specimens, ASTM International, West Conshohocken, PA, 2011.
- [27] ASTM NACE/ASTMG31 – 12a Standard Guide for Laboratory Immersion Corrosion Testing of Metals, ASTM International, West Conshohocken, PA, 2012.
- [28] G. Sauerbrey, Verwendung von Schwingquarzen zur Wägung dünner Schichten und zur Mikrowägung, *Z. Phys.* 155 (1959) 206–222.
- [29] ASTM G46-94(2013) Standard Guide for Examination and Evaluation of Pitting Corrosion, ASTM International, West Conshohocken, PA, 2013.
- [30] R. McDonald, S. Shrader, D. Stull, Vapor pressures and freezing points of thirty pure organic compounds, *J. Chem. Eng. Data* 4 (1959) 311–313.
- [31] NIST Chemistry WebBook, NIST Standard Reference Database Number 69, National Institute of Standards and Technology, Gaithersburg, MD (retrieved 21.08.13).
- [32] J. Krisch, B. Szajani, Ethanol and acetic acid tolerance in free and immobilized cells of *Saccharomyces cerevisiae* and *Acetobacter aceti*, *Biotechnol. Lett.* 19 (1997) 525–528.
- [33] C. Leygraf, Atmospheric corrosion, *Encyclopedia of Electrochemistry*, Wiley-VCH, 2007.
- [34] M.M. Singh, A. Gupta, Corrosion behavior of mild steel in acetic acid solutions, *Corrosion* 56 (2000) 371–379.
- [35] G.W. Whitman, R.P. Russell, V.J. Altieri, Effect of hydrogen-ion concentration on the submerged corrosion of steel, *Ind. Eng. Chem.* 16 (1924) 665–670.
- [36] B. Little, R. Ray, A perspective on corrosion inhibition by biofilms, *Corrosion* 58 (2002) 424–428.
- [37] M.A. Javed, P.R. Stoddart, E.A. Palombo, S.L. McArthur, S.A. Wade, Inhibition or acceleration: bacterial test media can determine the course of microbiologically influenced corrosion, *Corros. Sci.* 86 (2014) 149–158.
- [38] G. Grass, C. Rensing, M. Solioz, Metallic copper as an antimicrobial surface, *Appl. Environ. Microbiol.* 77 (2011) 1541–1547.
- [39] Z. Lin, D. Han, S. Li, Study on thermal decomposition of copper(II) acetate monohydrate in air, *J. Therm. Anal. Calorim.* 107 (2012) 471–475.
- [40] R.G. Ford, P.M. Bertsch, Distinguishing between surface and bulk dehydration–dehydroxylation reactions in synthetic goethites by high-resolution thermogravimetric analysis, *Clays Clay Miner.* 47 (1999) 329–337.
- [41] U. Evans, Electrochemical mechanism of atmospheric rusting, *Nature* 206 (1965) 980–982.
- [42] M. Legodi, D. De Waal, The preparation of magnetite, goethite, hematite and maghemite of pigment quality from mill scale iron waste, *Dyes Pigm.* 74 (2007) 161–168.
- [43] D.A. Jones, *Principles and Prevention of Corrosion*, Prentice-Hall Inc., NJ, 1996.
- [44] E. Escalante, J. Kruger, Stress corrosion cracking of pure copper, *J. Electrochem. Soc.* 118 (1971) 1062–1066.
- [45] L.A. Jain, Evaluation of the Propensity for Microbiologically Influenced Corrosion of Steels in Fuel Grade Ethanol Environments, PhD. Dissertation, Department of Metallurgical and Materials Engineering, Colorado School of Mines, 2011, pp. 269.
- [46] M. Desai, Corrosion inhibitors for copper, *Mater. Corros.* 23 (1972) 483–487.